RSC Advances

ROYAL SOCIETY OF CHEMISTRY

PAPER

View Article Online
View Journal | View Issue

Cite this: *RSC Adv.*, 2020, **10**, 45149

Synthesis of free-standing ternary Rh–Pt–SnO_2-carbon nanotube nanostructures as a highly active and robust catalyst for ethanol oxidation†

Haixia Wang, Shuhui Sun and Mohamed Mohamedi *

The rational design of durable materials is an important issue for improving the performance of electrocatalysts towards the ethanol oxidation reaction (EOR). In this work, binderless thin nanostructured layers of SnO_2, Pt, Rh, bilayers of Pt/SnO_2, Rh/Pt and tri-layers of Rh (*ca.* 10 nm thickness)/PtSnO_2 are directly grown by pulsed laser deposition onto carbon nanotubes (CNTs). SEM analysis shows that CNTs are perfectly coated with the catalysts. The onset potentials of the CO stripping and EOR indicate that Rh/Pt/SnO_2 is the most active for the CO and the EOR. The incorporation of the CNTs in the catalyst layer is outstandingly beneficial to both the catalytic current activity and the durability. Indeed Rh/Pt/SnO_2/CNT delivers mass activity as high as 213.42 mA mg^{-1}_{Pt}. Moreover, Rh/Pt/SnO_2/CNT demonstrates not only the lowest poisoning rate (by intermediate species, such as adsorbed CO) but also the highest durability current of 132.17 mA mg^{-1}_{Pt} far superior to CNT-free Rh/Pt/SnO_2/CP (58.33 mA mg^{-1}_{Pt}). XPS shows that SnO_2, Pt and Rh are all present at the surface of Rh/Pt/SnO_2/CNT, the presence of two oxophilic materials like SnO_2 and Rh, implies an earlier source of OH_{ads}-species, which facilitates the oxidation of CO and assuming a second contribution from Rh is to enhance the cleavage of the C–C bond for the complete oxidation of ethanol. The 3D porous and binderless structure, the low amount of the noble catalyst, the excellent electroactivity and durability of the Rh_5/PtSnO_2/CNT/CP composite represents an important step in advancing its use as an anode in commercial applications in DEFC.

Received 27th November 2020
Accepted 15th December 2020

DOI: 10.1039/d0ra10030g

rsc.li/rsc-advances

1. Introduction

Clean energy has attracted enormous attention over the past decades, due to the consumption of the depleted fossil fuels and environmental pollution. In this respect, fuel cells, an electrochemical energy device directly converting chemical energy into electrical energy, have been prevalently regarded as eco-friendly energy conversion equipment applied to portable electronics, automobiles, and stationary applications.[1] Among assorted fuel cells, Direct Ethanol Fuel Cells (DEFCs) play a prominent role both in environmental protection and reasonable use of resources,[2] which are the two imperative problems for sustainable development of the national economy. As a fuel, ethanol has distinct advantages, higher energy densities (8.01 kW h kg^{-1} *vs.* 6.09 kW h kg^{-1} for methanol) but cheap in price, lower permeability than methanol, high boiling point for safe storage and easy transportation and great potential for scale-up production through fermentation processes from renewable sources (*e.g.* sugar, starch and cellulose) or from non-conventional sources like food waste, agricultural waste and wood waste making ethanol a suitable fuel for green fuel cell technology.

Yet, the commercialization of DEFCs is hindered by the incomplete oxidation of ethanol to CO_2 due to the low actual anode catalyst activities, which decreases the fuel efficiency. Indeed, platinum, the most, commonly used catalyst for the application of fuel cells rather catalyzes the reaction to produce acetic acid or acetaldehyde.[3] The main challenge in developing catalysts for EOR is to discover multicomponent systems that enable dehydrogenation, C–C bond cleavage and CO_{ads} oxidation in order that the total conversion of ethanol to CO_2 to take place.[4,5]

In order to boost up the catalytic activity towards EOR, a large number of studies have indicated that oxophilic metal Sn or SnO_2 when added to Pt have the best performance for the removal of strongly adsorbed CO from Pt because of the strong affinity for water molecules.[6–12] Indeed, these studies showed that in the Pt–Sn or Pt–SnO_2 systems, the overall reaction rate of EOR increased, the onset potential of oxidation decreased and the peak current density was enhanced. Such improved performance was explained by the fact that metal oxide species stabilize Pt nanoparticle dispersions, and they are prone to

Énergie, Matériaux et Télécommunications (EMT), Institut National de la Recherche Scientifique (INRS), 1650 Boulevard Lionel Boulet, Varennes, Quebec, J3X 1S2, Canada. E-mail: mohamedi@emt.inrs.ca

† Electronic supplementary information (ESI) available. See DOI: 10.1039/d0ra10030g

adsorption of higher number of OH adsorbed species at lower potentials (bifunctional effect), which facilitate the CO electro-oxidation process during the EOR. Nevertheless, *in situ* Fourier transform infrared spectroscopy (FTIRS) and differential electrochemical mass spectroscopy (DEMS) studies revealed that with the PtSn-based catalysts, the oxidation of ethanol to CO_2 was not complete because the cleavage of the C–C bond was not accomplished with these catalysts.[13]

It became clear then that a third component capable of splitting the C–C bond is required and up to now only rhodium (Rh) has shown that potential capability.[14–21] Li *et al.* used a modified polyol method to synthesize a series of ternary PtRh–SnO_2/C catalysts with the atomic ratio Pt : Rh : Sn = 3 : 1 : x (x = 2,3,4,5, 6) and studied their catalytic activity toward EOR.[22] The results showed $Pt_3Rh_1Sn_4$ not only had the highest current density, the most negative onset potential, but also had the capability to break the C–C. Li and co-workers later considered SnO_2 instead of Sn and observed that the catalytic activity of the catalysts towards EOR decreased in the order of $PtRhSnO_2$ > $PtSnO_2$ > Pt > PtRh > Rh > $RhSnO_2$.[23] *In situ* infrared reflection-absorption spectroscopy (IRRAS) results demonstrated that Rh can split the C–C bond and the selectivity of the catalysts to CO_2 decreased in the order of: $PtRhSnO_2$ ~ $RhSnO_2$ > PtRh > Pt > $PtSnO_2$ ~ Rh. Adzic group synthesized multimetallic nanoislands MM'/SnO_2 (MM' = PtIr, PtRh, IrRh, PtIrRh) and they found that $PtRh/SnO_2$/C catalysts ($PtRh_{1/3}/SnO_2$/C and $PtRh_{1/2}/SnO_2$/C) can break the C–C bond of ethanol in $HClO_4$ solution at room temperature, and the catalyst $PtRh/SnO_2$/C had the highest ethanol conversion efficiency as well.[24]

In addition, it is well known that the supporting material can significantly affect the electrochemical performance of a catalyst. Owing to their high electronic conductivity nanostructured carbons such as carbon nanofibers (CNFs), carbon nanotubes (CNTs), carbon nanospheres (CNs) and graphene have shown to enhance the conductivity of several catalysts including metal, metal oxides and alloys.[25,26] Such conductivity enhancement results in improved electrocatalytic activity towards the oxidation of small organic molecules (formic acid, methanol, ethanol) of interest to fuel cell technologies. Particularly CNTs are suitable material for the electrode/catalyst supports due to their high surface area (250 $m^2\ g^{-1}$), excellent electrical conductivity (3.5×10^5 S m^{-1}), structural stability, mechanical toughness (fracture energy above 80 J g^{-1}).[27–29] Additionally, the long-term durability of the catalyst is critical during fuel cell operation, and Pt-based catalysts are extremely prone to segregation or detachment primarily due to corrosion of the carbon black supports the conventional carbon black (Vulcan XC-72).[30,31] This results in a diminution in the number of active sites on Pt, which considerably decreases its efficiency for fuel cells electrochemical reactions. CNTs due to their extraordinary mechanical properties, high degrees of crystallinity, as well as high chemical stability and higher corrosion resistance performance in acidic environment compared to activated carbons could drastically boost the stability of Pt-based catalysts.

In line of developing further the electrochemical performance of the multicomponent $Rh/Pt/SnO_2$ catalysts for practical applications in fuel cells particularly DEFCs, it is necessary to employ a better catalyst support such as CNTs. However, preparing $Rh/Pt/SnO_2$ porous nanostructures onto tortuous solid supports such as CNTs and expose the catalytically clean metal surface for reactivity is challenging. The present work addresses that task and reports the synthesis with PLD of $Rh/Pt/SnO_2$ *tri*-layered nanostructures onto CNTs, which were synthesized by chemical vapor deposition (CVD) technique. To obtain a full picture of the effect of CNTs on the electroactivity of $Rh/Pt/SnO_2$ catalyst in relation with the physico-chemical properties, a rigorous methodology was adopted here:

(i) In order to investigate the effect of CNTs on each element constituting the multicomponent $Rh/Pt/SnO_2$ electrocatalyst, SnO_2, Pt, Rh, Pt/SnO_2, Rh/Pt and $Rh/Pt/SnO_2$ materials are grown onto CNTs. The effects of CNTs on the structural properties of these materials are studied with scanning electron microscopy (SEM), X-ray diffraction (XRD) and X-ray photoelectron spectroscopy (XPS).

(ii) The effect of the presence of CNTs on the tolerance to CO-poisoning is studied by anodic stripping voltammetry (ASV).

(iii) The catalysts are evaluated for their electroactivity towards EOR with linear scan voltammetry (LSV), whereas their durability is studied with chronoamperometry (CA).

(iv) The importance of the integration of CNTs in the ternary $Rh/Pt/SnO_2$ catalyst structure is also demonstrated by comparison with the CP support.

2. Experimental

2.1 Chemicals and materials

The current collector is an untreated carbon paper (CP, Toray), commonly employed in fuel cells as the gas diffusion layer (GDL). PLD targets SnO_2 (99.99%), Rh (99.8%) and Pt (99.99%) are purchased from Kurt J. Lesker Co. Sulfuric acid (96% purity) and ethanol (100% purity) are purchased from Agros Organics and Commercial Alcohols Inc., respectively.

2.2 Synthesis

2.2.1 Synthesis of CNTs. CNTs were grown at 700 °C by chemical vapor deposition (CVD) using Ni as catalyst deposited by PLD onto CP substrate, and acetylene (carbon source), hydrogen and argon (gas carrier) gases at flow rates of 30, 140 and 100 sccm, respectively. Full details regarding the synthesis of CNTs can be found elsewhere.[32]

2.2.2 Synthesis of catalysts onto CNTs. PLD was carried out at room temperature and ablating the pure targets by means of a pulsed KrF excimer laser (λ = 248 nm, pulse width τ = 17 ns and repetition rate = 50 Hz) using Helium as background gas. Prior to synthesis, the pressure in a stainless-steel ultra-high vacuum chamber was pumped to a base pressure of 4×10^{-5} Torr by a turbo bump. Then the chamber was filled with high-purity He (Helium N5.0, Praxair) at the established He background pressure. The substrate-to-target distance was set to 5 cm. Onto CNTs, we synthesized mono-layered catalysts SnO_2, Pt and Rh; *bi*-layered Pt/SnO_2, Rh_5/Pt; and *tri*-layered catalysts $Rh_5/Pt/SnO_2$. Main deposition parameters related to the growth conditions by PLD of SnO_2, Pt, and Rh are summarized in Table

Table 1 The PLD deposition parameters of SnO_2, Pt and Rh

	SnO_2	Pt	Rh
He background pressure	0.5	2	2
Laser fluence (J cm^{-2})	4	4	7
Number of laser pulses (N_{lp} 10^3)	20	50	5

1. Further understanding of the PLD setup and its working principle are given elsewhere.[33] We synthesized six electrocatalysts: unitary catalysts SnO_2, Pt, Rh; binary catalysts Pt/SnO_2, Rh_5/Pt, and ternary catalyst Rh_5/Pt/SnO_2. Here Rh_5 denotes Rh deposited with 5000 laser pulses producing a film thickness of *ca.* 10 nm.[34] The loading of Pt was 120 μg cm^{-2} (measured by neutron activation analysis, NAA).

2.3 Materials characterization

The surface morphology of the as-prepared samples was examined by SEM (JEOL, JSM 7401 F apparatus) operated at an accelerating voltage of 10 kV in the secondary electron mode and a working distance of 10 mm. The measurements were performed in a working pressure of 8×10^{-6} mbar. The crystalline structure of all samples was determined by XRD using Bruker D8 Advance diffractometer equipped with a Cu Kα source ($\lambda = 1.5406$ Å). All diffractograms were obtained in the Grazing Incidence Diffraction (GID) scan mode with a low incident angle of 2° and a 2θ angular step size of 0.04° with an acquisition time of 4 s per step in the range of 20–90°. XPS measurements were carried out *via* a VG Escalab 220i-XL set with Al Kα source (1486.6 eV). The anode was operated at 10 kV and 20 mA. The pass energy of the analyzer was set at 20 eV. The base pressure of the system was 10^{-9} mbar. All samples were analyzed with a spot size of 250 × 1000 μm located approximately in the center of the sample. A survey spectrum ranging from 0 to 1350 eV was first acquired, and then higher resolution multiplex scan spectra (C 1s, O 1s, Sn 3d, Pt 4f and Rh 3d core levels) were obtained. Quantification of the elements was performed with Casa XPS software version 2.3.19 Pro 1.0 (Casa Software Ltd.) by fitting the core level spectra after a Shirley background removal. The metallic components of the Pt 4f and Rh 3d region were fitted using a Gaussian/Lorentzian asymmetrically modified line shape, and symmetrical Gaussian/Lorentzian were used to fit other components. The C 1s core level peak at 284.6 eV, resulting from hydrocarbon contaminants at the surface, was taken as an internal reference binding energy for charge correction.

2.4 Electrochemical characterization

2.4.1 Electroactivity. The electrocatalytic characterization was first evaluated by cyclic voltammetry (CV) in Ar-saturated 0.5 M H_2SO_4 solutions using a three-compartment electrochemical cell including an Ag/AgCl, 4 M NaCl reference electrode, a platinum coil counter electrode and the synthesized samples as working electrodes. Prior to each electrochemical experiment, dissolved oxygen was purged from the electrolytic solution by bubbling pure argon for 30 and 15 min, respectively in 0.5 M H_2SO_4 and 0.5 M H_2SO_4 containing 1 M C_2H_5OH electrolytes. To estimate electrochemically active surface area (*ESA*) of the catalysts, the working electrode was first activated by multiple CVs at 50 mV s^{-1} scan rate between −0.2 V and 1 V in 0.5 M H_2SO_4 solution until reaching a stationary CV profile, which was used to measure the *ESA* (as described a little later in the results and discussion section). For the EOR studies, LSVs were conducted at the potential range of $0 \leq E \leq 1$ V with quasi-steady state potential scan rate of 5 mV s^{-1}. Durability testing was performed by recording CA curves at an anodic potential of 0.6 V upon a period of 3600 s. All the currents are normalized by

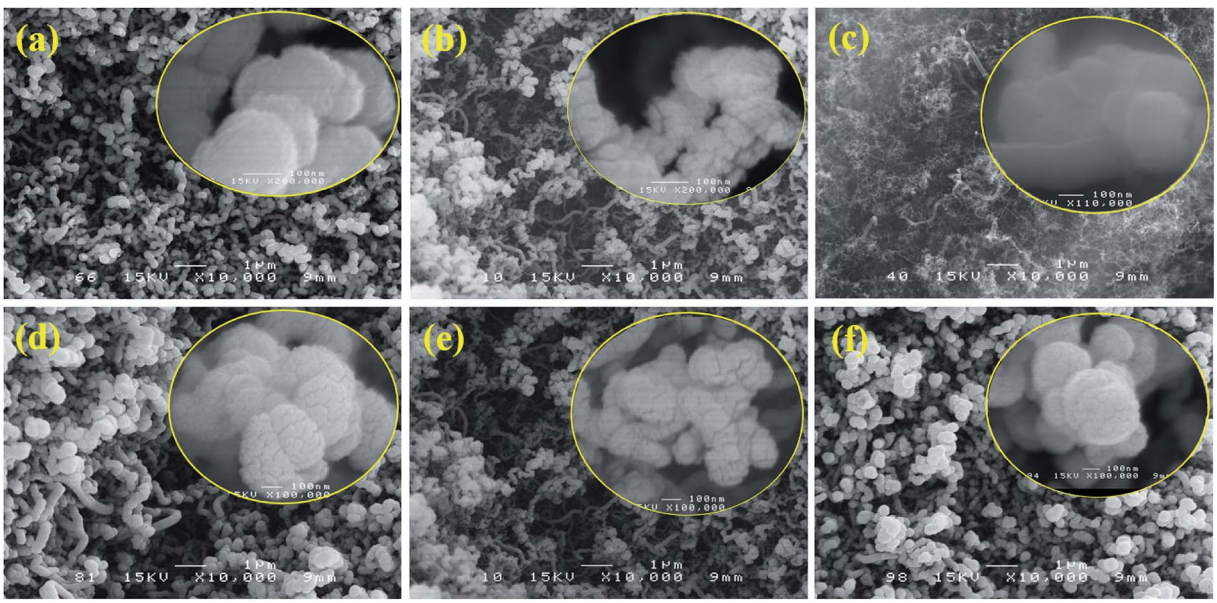

Fig. 1 SEM images of PLD synthesized layers. (a) SnO_2/CNT, (b) Pt/CNT, (c) Rh_5/CNT, (d) Pt/SnO_2/CNT, (e) Rh_5/Pt/CNT, (f) Rh_5/Pt/SnO_2/CNT.

either the geometric area of the working electrode (0.308 cm^2) or by the mass loading of Pt. All the experiments were conducted at room temperature (22 ± 0.5 °C) and data acquisition were acquired with a computer-controlled potentiostat-galvanostat (Autolab, PGSTAT 20, GPES).

2.4.2 Tolerance to CO poisoning. CO stripping experiments were conducted by the following steps. After deaerated the 0.5 M H_2SO_4 solution by bubbling pure N_2 for 30 min, the electrode surface was cleaned and completely activated by potential cycling to steady state in the solution for 30 cycles with a scan rate of 50 mV s^{-1} within the range from −0.2 V to 1 V *vs.* Ag/AgCl under continuing flow of N_2. Then the pure CO (99.5%) was purged into the above-mentioned solution at a polarized potential of 0 V *vs.* Ag/AgCl for 30 min to ensure CO adsorption on the surface of the working electrode. The potential being remained constant, pure N_2 stream was bubbled for 30 min to remove redundant CO dissolved in the solution. Subsequently, the CO stripping was achieved using ASV.

3. Results and discussion

3.1 Physico-chemical characterization

Fig. S1 in the ESI† presents SEM images of the bare CP substrate and the CNTs grown on CP. As can be seen from Fig. S1a, b,† the carbon fibers of CP are straight with a diameter ranging from 5 to 8 μm. While the CNTs (Fig. S1c, d†) are crisscrossing and involute. The diameter of CNT is measured around 20–50 nm. The surface morphology of all PLD-prepared catalysts onto CNTs is shown in Fig. 1. The diameter of SnO_2/CNT (Fig. 1a) is between 160 and 200 nm due to the deposition of SnO_2 coating, while that of Pt/CNT (Fig. 1b) ranges from 70 to 100 nm with a porous morphology. In contrast, Rh_5/CNT (Fig. 1c) film is quite smooth, probably because Rh nanoparticles are extraordinarily small. Pt/SnO_2/CNT (Fig. 1d) displays a cerebrum shape with the diameter of 200–250 nm. Rh_5/Pt/CNT (Fig. 1e) exhibits similar appearance with Pt/CNT, but the former's surface is less rough than the latter. Rh_5/Pt/SnO_2/CNT (Fig. 1f) displays a porous cauliflower-like structure. It is acknowledged that 3D porous nanostructures comprised of intimately interconnected catalyst particles or filaments offers a larger surface area and facilitates the efficient transport of reactants and products. This could provide enhanced electroactivity compared to dispersed nanoparticles catalysts.[35,36]

Fig. 2 shows the XRD diffraction patterns of SnO_2/CNT, Pt/CNT, Rh_5/CNT, Pt/SnO_2/CNT, Rh_5/Pt/CNT and Rh_5/Pt/SnO_2/CNT catalysts. XRD spectrum of pristine CNTs is shown in Fig. S2† for referencing. As it can be seen, no SnO_2 diffraction peaks are observed probably because SnO_2 is in the form of quite small nanoparticles or as an amorphous structure. The existence of SnO_2 could be however evidenced by XPS analysis hereafter. The corresponding XRD patterns of Pt based catalysts show four diffraction peaks at *ca.* 39.8°, 46.2°, 67.5° and 81.3°, which can be indexed respectively to (111), (211), (100) and (311) planes (JCPDS PDF No. 04-0802), characteristic of a face-centered cubic (fcc) structure. No Rh diffraction peaks are detected in Rh-based catalysts, it may be because of the ultra-low content of rhodium or Rh exists as amorphous state.[34]

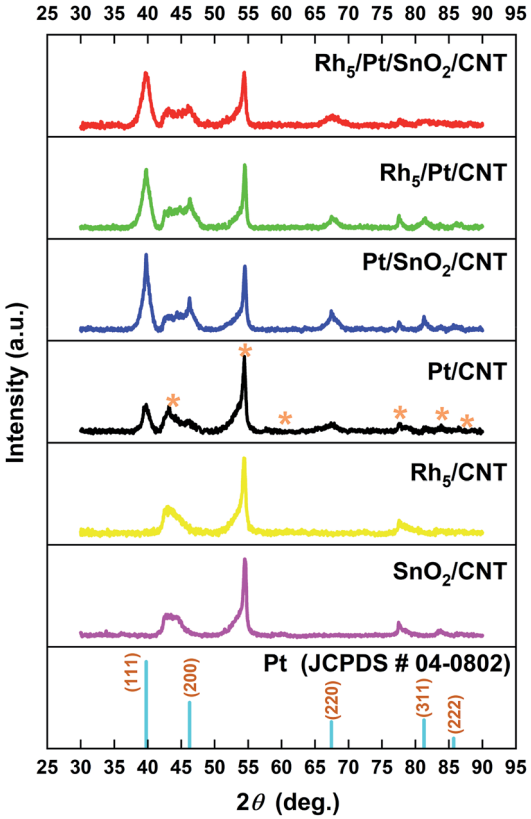

Fig. 2 XRD patterns of PLD synthesized catalysts onto CNTs support. The diffraction peaks of the CNTs substrate are identified with (*) in the patterns.

The most intensive diffraction peak Pt (111) is selected to calculate the lattice constant (a), the interplanar space d_{111} and the average crystallite size (CS) of Pt nanoparticles by Bragg's law and Debye–Scherrer equation, respectively. The corresponding results are summarized in Table S1,† which shows that with the addition of SnO_2 and Rh to Pt, the 2θ slight downshifted and the corresponding lattice constant expanded in comparison with these of Pt/CNT (39.78° and 3.922 Å, respectively). This indicates the strong interaction between SnO_2 (Rh) and Pt. Meanwhile, CS of Pt became smaller, due to the high dispersion of SnO_2.

XPS survey scan and high-resolution C 1s and O 1s core-levels of the pristine CNTs support are reported in Fig. S3† as reference. The XPS survey spectra shown in Fig. S4† demonstrate that the surface of the catalysts exclusively consist of Rh, Pt, Sn, O and C elements. The C1s peak as shown in Fig. S5† fitted to Voigt functions with 70% Gaussian and 30% Lorentzian could be well resolved into five components centered at binding energies (BEs) of 284.5 eV, ~285.5 eV, ~286.6 eV, ~287.8 eV and ~288.9 eV were assigned to C=C, C–C, epoxide group C–O, to carbonyl carbon (C=O) and carboxylate carbon (O=C–O), respectively.[37–39]

High-resolution XPS spectra in the corresponding regions: (a) O 1s, (b) Sn 3d (c) Pt 4f and (d) Rh 3d are reported in Fig. 3. The O 1s spectra of all samples are deconvoluted into 2 to 4 components, indicating the presence of oxygen in different chemical

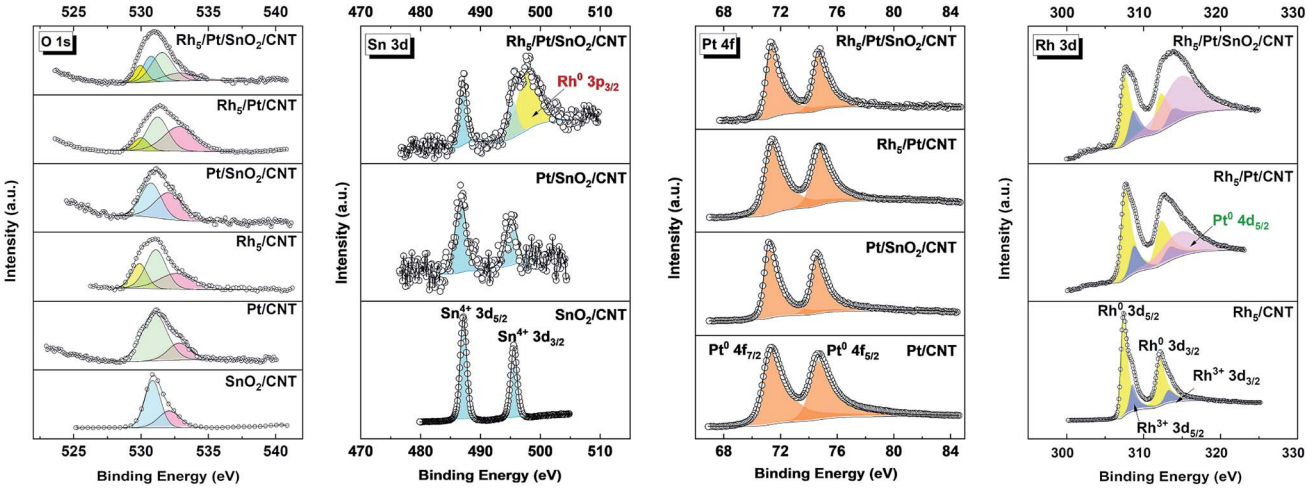

Fig. 3 High-resolution XPS of O 1s, Sn 3d, Pt 4f and Rh 3d core-levels.

states. In the case of Pt/CNT, the O 1s spectrum can be resolved into two peaks, the lower peak located at *ca.* 531.2 eV is related to the surface C=O like species of carboxyl groups and the higher *BE* peak positioned at around 532.9 eV is associated with other oxygen-containing surface functional groups, such as C–O bond.[40] In SnO_2/CNT and Pt/SnO_2/CNT, the O 1s is plotted with two peaks; one peak centered at high *BE*s (*ca.* 532.7 eV) is related to C–O bond, the other peak appeared at lower *BE*s (*ca.* 530.7–530.8 eV) is assigned to Sn^{4+}–O species in the SnO_2 phase.[41] For the O 1s spectra of the Rh-based catalysts, the bonds of Rh–O (*ca.* 529.9 eV), C=O (*ca.* 531.4 eV) and C–O (*ca.* 532.8 eV) are all well observed. Interestingly, an additional Sn–O bond (530.8 eV) is detected in Rh_5/Pt/SnO_2/CNT, which can obviously be attributed to oxygen in SnO_2. It implies SnO_2 and Rh coexist on the surface of the ternary Rh_5/Pt/SnO_2/CNT. In all SnO_2-based catalysts, the Sn 3d spectra (Fig. 3) reveals two prominent peaks with a spin–orbit splitting of 8.41 eV related to $3d_{5/2}$ and $3d_{3/2}$ at *ca.* 486.70–487.15 eV and *ca.* 495.11–495.5 eV, respectively corresponding to the *BE*s of Sn(IV) in SnO_2.[42] In addition, the symmetric Sn 3d spectra manifested the presence of one chemical environment for tin atom. It is noteworthy that Rh $3p_{3/2}$ is observed in the Sn 3d spectrum of Rh_5/Pt/SnO_2/CNT, which further demonstrates SnO_2 and Rh coexisted on the surface of this ternary. Analyzing the Pt 4f region in high solution (Fig. 3), the characteristic doublet of the Pt for the $4f_{7/2}$ and $4f_{5/2}$ orbitals is perceptible in all Pt based catalysts. The Pt 4f spectrum is fitted by one resolved doublet with a *BE* separation of *ca.* 3.33 eV. The lower *BE* doublet (Pt $4f_{7/2}$) and the higher *BE* doublet (Pt $4f_{5/2}$) are positioned at 71.20–71.33 eV and 74.53–74.66 eV, respectively, which corresponded to metallic state Pt^0. The Rh 3d was plotted with two spin–orbit doublets with peak separation of 4.74 eV (Fig. 3). The first predominant doublet at lower *BE*s of 307.42 eV and 312.18 eV are assigned to Rh $3d_{5/2}$ and Rh $3d_{3/2}$, respectively. The second doublet, with lower intensity located at higher *BE*s (308.78 eV and 313.42 eV) corresponds to rhodium oxide species Rh_2O_3. In Rh_5/Pt/SnO_2/CNT and Rh_5/Pt/CNT, there is another peak at *ca.* 314. 20 eV overlapped with Rh $3d_{3/2}$, which corresponds to the *BE* of Pt $4d_{5/2}$.[16]

The evolution of *BE*s of Sn 3d, Pt 4f and Rh 3d in the corresponding SnO_2, Pt- and Rh-based catalysts are summarized in Fig. S6.† As displayed, the *BE*s of Pt $4f_{7/2}$ in Pt/SnO_2/CNT (71.18 eV) slightly shifted to lower *BE*s compared with Pt/CNT (71.22 eV), which was consistent with previous reports.[43–45] Intrinsically, the downshift of Pt 4f originated from the increasing of electron density around the Pt sites. The Pt with increased electron density is less prone to oxidation, consequently weakening chemisorption energy with oxygen containing species and enhancing the electrocatalytic activity of the catalyst.[46] Concurrently, the *BE* of Sn $3d_{5/2}$ shifts by 0.4 eV negatively with respect to SnO_2/CNT (487.15 eV). These *BE*s shift can be attributed to the strong metal-substrate interaction (SMSI) between Pt and SnO_2 or size effects.[47] On the other hand, the *BE* of Pt 4f in Rh_5/Pt/CNT (71.13 eV) downshifted by 0.1 eV, whereas it upshifted by 0.1 eV in the Rh_5/Pt/SnO_2/CNT. Meanwhile, the corresponding Rh 3d respectively upshifted 0.1 eV and 0.34 eV, respectively in comparison with Rh_5/CNT (307.38 eV). The group of Nørskov also reported about the upshift of Rh 3d when Rh was on the top of Pt.[48,49] This may be related to size effects as well as the electronic effects arising from the incorporation of Rh atoms to Pt, or to the synergic effect between Pt, Rh and SnO_2. The surface atomic composition of all the catalysts is summarized in Table S2.† In Pt/SnO_2/CNT, the atomic ratio between SnO_2 and Pt was 0.15 : 1, the ratio Pt : Rh = 1 : 0.6 in Rh_5/Pt/CNT and the ratio SnO_2 : Pt : Rh = 0.15 : 1 : 0.67 in Rh_5/Pt/SnO_2/CNT.

3.2 Electrochemical characterization

Fig. 4 presents the voltammetric profiles of SnO_2/CNT, Pt/CNT, Pt/SnO_2/CNT, Rh_5/Pt/CNT and Rh_5/Pt/SnO_2/CNT electrodes. As shown in Fig. 4a, there was no hydrogen adsorption/desorption (H_{ads}/H_{des}) region in SnO_2/CNT. The Pt/CNT displayed a typical Pt H_{ads}/H_{des} region (−0.17–0.07 V) with well-defined peaks, followed by a broad and narrow double layer region (DL, 0.07–0.58 V), and an oxide region (O-region) where the formation/reduction of surface oxide take place.[50–52] At the Pt/SnO_2/CNT

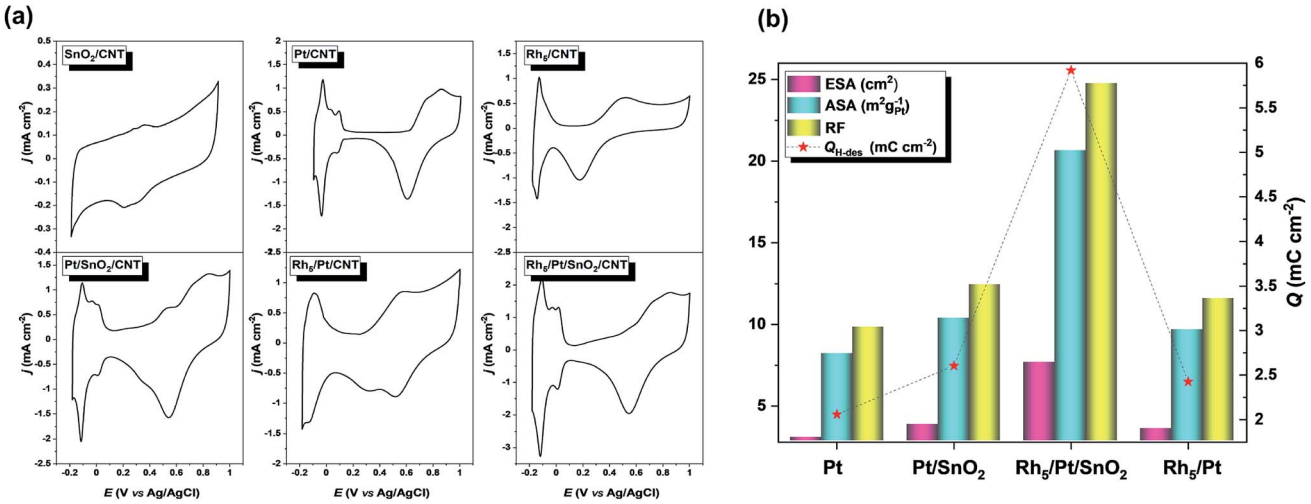

Fig. 4 (a) Cyclic voltammograms in 0.5 M H_2SO_4 solution recorded with a scan rate of 50 mV s^{-1}. (b) *ESA*, *ASA*, *RF* and *Q* estimated from (a).

catalyst, the DL window became narrow, but the capacitive current increased. On the other hand, the onset potential of surface oxides formation and the peak potential surface oxides reduction shifted negatively as compared to Pt/CNT. Similar change is also noticed in Rh-based catalysts (*e.g.* Rh_5/Pt/CNT and Rh_5/Pt/SnO_2/CNT). This phenomenon can be attributed to the oxophilic character of Sn and Rh.[53]

The electrochemically active surface area ($ESA = Q_H/Q_{ref}$) corresponding to each Pt-based electrocatalyst was estimated using the electric charge for the hydrogen desorption (Q_H) wave correlated with a monolayer hydrogen adsorbed on polycrystalline platinum (Q_{ref} = 0.21 μC cm^{-2}).[54] In addition, the area specific activity ($ASA = Q_H/(Q_{ref} \times m_{Pt} \times A_g)$ to generate mass activity and the roughness factor ($RF = ESA/A_g$) were also analyzed. Here m_{Pt} and A_g denote the Pt mass loading (120 μg cm^{-2}) and the geometric electrode area (0.308 cm^2), respectively. As calculated *ESA*, *ASA* and *RF* are gathered in Fig. 4b, which exhibits a volcano-shaped profile shows that the electroactivity of Rh_5/Pt/SnO_2/CNT by far was superior to the other electrocatalysts.

3.2.1 Electrocatalytic activity towards ethanol oxidation. LSV was carried out in the solution of 0.5 M H_2SO_4 + 1 M C_2H_5OH to evaluate the catalytic activity of the as-prepared electrocatalysts towards ethanol electrooxidation. As illustrated in Fig. 5a, the current densities on SnO_2/CNT and Rh_5/CNT were extremely low, it indicated and in agreement with the literature that SnO_2 or Rh alone are not electroactive towards the EOR.[19,55] At the Pt-based catalysts, the current was low initially and the hydrogen adsorption feature was hindered by the accumulated poisoning species (*e.g.* CO and CH_x) resulting from the dissociation of the adsorbed ethanol, in either linearly bonded or bridge bonded to Pt surface.[56] The peak current density j_p and onset potential E_{onset} of EOR are depicted in Fig. 5b. An increment of the peak current and a diminution of E_{onset} were observed after adding SnO_2 and Rh to Pt. The reduced E_{onset} can be ascribed to the *bi*-functional mechanism

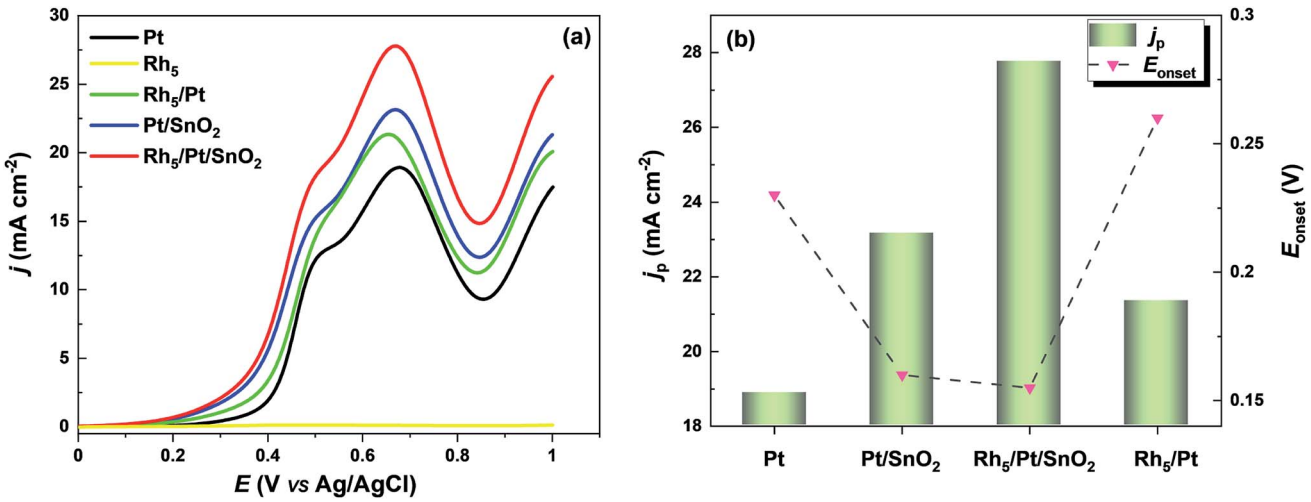

Fig. 5 (a) Electroactivity of electrocatalysts toward EOR. LSVs recorded in 1 M C_2H_5OH + 0.5 M H_2SO_4 solution taken with a scan rate of 5 mV s^{-1}. (b) j_p and E_{onset} values extracted from (a).

in which the hydrophilic SnO_2 (Rh) provides OH species at lower potentials accelerating by that the oxidation of CO-like intermediates and therefore freeing Pt sites for further ethanol dehydrogenation. The $Rh_5/Pt/SnO_2/CNT$ demonstrated the best catalytic activity toward EOR in terms of the lowest E_{onset} of 0.16 V and the highest j_p of 27.77 mA cm^{-2}. In addition, the value of j at 0.45 V can be used as an arbitrary criterion to further compare the current catalytic activity at potentials lower than the peak potential. Hence, from LSVs of Fig. 5a, j@0.45 V was found as follows: 14.31, 12.19, 9.20 and 7.37 mA cm^{-2} for $Rh_5/Pt/SnO_2/CNT$, $Pt/SnO_2/CNT$, $Rh_5/Pt/CNT$ and Pt/CNT, respectively.

With respect to practical applications, the crucial criterion for a good catalyst is having a good anti-poisoning ability and delivering high steady-state currents at a certain fixed potential during EOR. Fig. 6a shows the current density–time (j–t) curves of all as-prepared catalysts for EOR at 0.6 V upon 3600 s testing. It was noticed in all the CA profiles, j rose sharply in the first 10 s, then dropped rapidly and ultimately reached a steady state within 500 s. The first current density rise is due to the double-layer charging effect. The initial fast decay was caused by the rapid increase of the surface coverage by intermediate species, such as adsorbed CO during EOR.[57] As shown in Fig. 6a, $Rh_5/Pt/SnO_2/CNT$ exhibited the highest steady state current density j_{ss} (15.86 mA cm^{-2}), followed by $Pt/SnO_2/CNT$ (13.86 mA cm^{-2}), then $Rh_5/Pt/CNT$ (11.59) and Pt/CNT (7.12 mA cm^{-2}). The stability efficiency (j_{ss}/j_0, where j_0 is the initial current density at $t = 0$) and the decrement of the current density $(j_0 - j_{ss})/j_0$ are displayed in Fig. 6b. It is clear that the $Rh_5/Pt/SnO_2/CNT$ delivered the highest efficiency and lowest current attenuation throughout the experiment.

3.2.2 Electrocatalytic CO oxidation activity. Fig. 7a shows ASVs of the adsorbed CO at the PLD-synthesized electrocatalysts in 0.5 M H_2SO_4 electrolyte, and the full CO stripping cyclic voltammograms are displayed in Fig. S7.† A sharp CO oxidation peak (CO_{ox}) was observed on Pt/CNT electrode, whereas a relatively blunt peak was present on Rh_5/CNT electrode. It is because of the CO mobility is slow on Rh.[34,58] After adding Rh to Pt, the CO_{ox} peak of $Rh_5/Pt/CNT$ became less sharp than Pt but broader than Rh_5/CNT. In the case of SnO_2/CNT, no CO_{ox} peak was observed, suggesting that SnO_2 alone is not prone to CO adsorption. Nevertheless, anchoring Pt particles on SnO_2, the CO stripping voltammogram developed into one broad wave spreading from 0.1 V to 0.5 V and one peak at 0.61 V. This can be considered that the low potential broad wave originated from the reaction of CO_{ads} with hydroxyl groups on SnO_2 adjacent to Pt sites, while the high potential peak came from the reaction of CO_{ads} with hydroxyl groups produced on pure Pt, which is analogous to what have been observed and interpreted for the $Pt/CeO_2/CNT$ and PtRu systems.[59,60] Similar ASV profile was observed in $Rh_5/Pt/SnO_2/CNT$ but at slightly lowest potentials and with current densities higher than those with $Pt/SnO_2/CNT$ electrocatalyst.

The area specific activity ($ASA_{CO\text{-}ox} = Q_{CO}/(0.42 \times m_{Pt} \times A_g)$) related to each Pt-based electrocatalyst was estimated. Here, 0.42 mC cm^{-2} represents the surface charges for linearly adsorbed CO.[61] Accordingly, $ASA_{CO\text{-}ox}$ for Pt/CNT, $Pt/SnO_2/CNT$, $Rh_5/Pt/SnO_2/CNT$, $Rh_5/Pt/CNT$ and Rh_5/CNT were found equal to 10.92, 13.70, 18.71 and 15.76 $m^2\ g^{-1}_{Pt}$, respectively. The corresponding CO_{ox} peak potential $E_{p\text{-}CO\text{-}ox}$ and onset potential $E_{onset\text{-}CO\text{-}ox}$ are summarized in Fig. 7b. The $E_{p\text{-}CO\text{-}ox}$ declined in sequence from Pt/CNT (0.67 V), $Pt/SnO_2/CNT$ (0.61 V), $Rh_5/Pt/CNT$ (0.62 V), $Rh_5/Pt/SnO_2/CNT$ (0.59 V) to Rh_5/CNT (0.55 V). Note that the $E_{p\text{-}CO\text{-}ox}$ shifted negatively with the addition of SnO_2 and Rh, which indicated that the addition of SnO_2 and Rh accelerated the CO oxidation at lower potentials. The $E_{onset\text{-}CO\text{-}ox}$ exhibited a trend similar to that observed with $E_{p\text{-}CO\text{-}ox}$. The $E_{onset\text{-}CO\text{-}ox}$ were much lower on $Rh_5/Pt/SnO_2/CNT$ (0.17 V) and $Pt/SnO_2/CNT$ (0.19 V) than that on Rh_5/CNT (0.49 V), $Rh_5/Pt/CNT$ (0.52 V) and Pt/CNT (0.57 V). These results imply that CO species are more readily removed on the surface of these SnO_2- and Rh-based Pt catalysts than Pt/CNT. Because SnO_2 and Rh

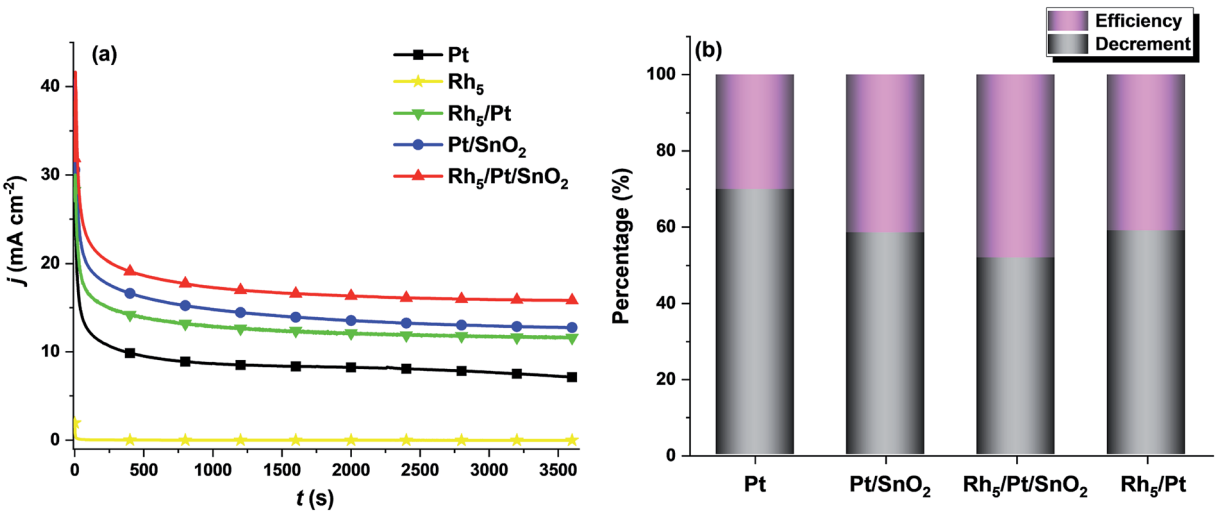

Fig. 6 (a) Durability evaluation by chronoamperometry of electrocatalysts recorded over 1 hour in 1 M C_2H_5OH + 0.5 M H_2SO_4 solution. (b) Efficiency and decrement.

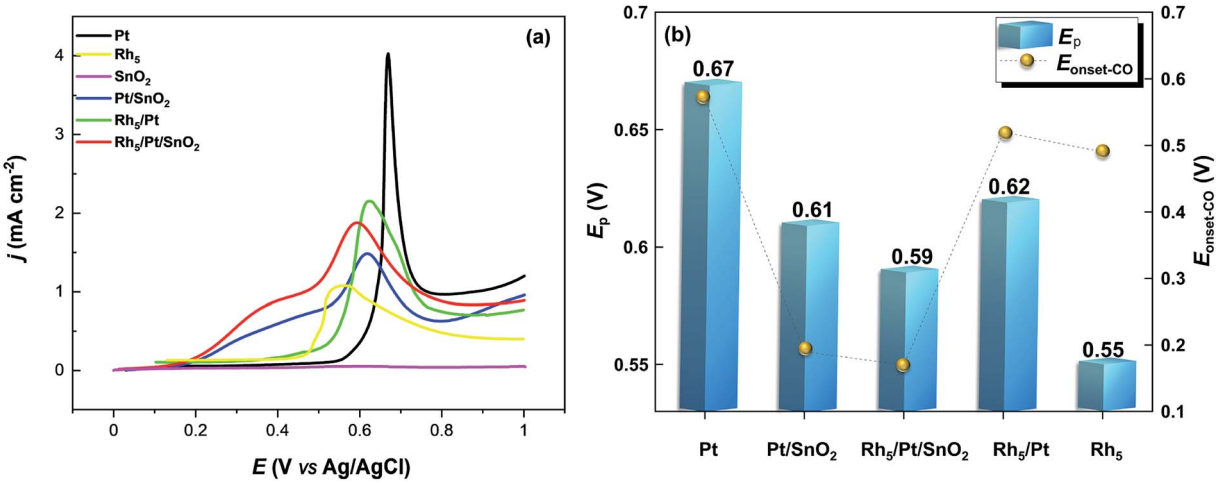

Fig. 7 (a) CO-stripping voltammetry in the base electrolyte 0.5 M H_2SO_4 recorded at 50 mV s^{-1}. (b) E_p and $E_{onset\text{-}CO}$ values extracted from (a).

Table 2 Comparative main electrochemical performance parameters

	Electroactivity		EOR			Durability			CO-oxidation
	ESA (cm^2)	*ASA* ($m^2\ g^{-1}$)	E_{onset} (V)	j_p (mA cm^{-2})	*MA*[a] (mA mg^{-1}_{Pt})	j_{ss} (mA cm^{-2})	*MA* (mA mg^{-1}_{Pt})	δ (% s^{-1})	$E_{onset\text{-}COox}$ (V)
$Rh_5/Pt/SnO_2/CP$	5.77	15.63	0.167	21.53	179.40	7.00	58.33	0.0099	0.17
$Rh_5/Pt/SnO_2/CNT$	6.35	17.20	0.160	27.77	213.42	15.86	132.17	0.0072	0.17

[a] Mass activity.

have high affinity for water, they can thus activate adsorbed water molecule to provide oxygen species at lower potentials and therefore increase the CO–OH coupling.

3.2.3 Role of carbon nanotubes. The effect of the carbon nanotubes can be discussed *versus* the benchmark CP support. Tables S3–S6† compare respectively the various electrochemical parameters obtained from electroactive surface area in H_2SO_4 solution, EOR from LSV, durability from CA and CO-tolerance at the various catalysts grown on CNTs with those grown on CP substrate. Table 2 focuses only on the ternary $Rh_5/Pt/SnO_2$ since this one has shown the best electrochemical performance. As can be seen, CNTs had no significant effect on either E_{onset} for the oxidation of ethanol or $E_{onset\text{-}CO\text{-}ox}$ for the oxidation of CO. This result is not surprising since CNTs do not catalyze these two electrochemical reactions. However, CNTs conferred substantial improvement in terms of surface electroactivity and current catalytic activity for the EOR. This demonstrates that CNTs enhanced the electrical conductivity of the catalyst and offered a better utilization of its nanoparticles for promoting the EOR. Yet, the remarkable contribution of the CNTs can be seen in the durability behavior, where the steady-state current activity upon time is 2.26 times higher than with CP as the support. The poisoning rates (δ% s^{-1}) calculated from CA curves for $t > 500$ s on the basis of the approach proposed by Jiang *et al.*,[62] clearly shows that CNTs offers a much better resistance to corrosion (Table 2).

4. Conclusions

In this work, free-standing nanostructured catalyst layers of SnO_2, Pt, Rh_5, Pt/SnO_2, Rh_5/Pt and $Rh_5/PtSnO_2$ were synthesized at room temperature by PLD directly on carbon nanotubes, which are grown directly on carbon paper substrate. Their physico-chemical properties as well as their electrocatalytic activity toward EOR and CO-tolerance were systematically investigated. SEM imaging revealed that the CNTs were uniformly coated with the catalysts. XRD analysis showed that Rh and SnO_2 expand the lattice parameter and interplanar space of Pt and reduced the crystallite size of Pt nanoparticles. XPS demonstrated that Pt and Rh were in metallic states whereas tin was in Sn^{4+} species. Electrochemical observations confirmed that Rh and SnO_2 alone were not active for EOR. But when incorporated with Pt, the electrocatalytic activity significantly improved, especially with the ternary $Rh_5/Pt/SnO_2/CNT$. Indeed, this catalyst exhibited the highest mass activity of 213.42 mA mg^{-1}_{Pt}, 1.35, 1.19, and 2.7 times higher than Pt/CNT, $Rh_5/Pt/SnO_2/CP$ and Pt/CP, respectively. Furthermore, the $Rh_5/Pt/SnO_2/CNT$ demonstrated not only the lowest poisoning rate (by intermediate species, such as adsorbed CO) but also delivered the highest stability current of 132.17 mA mg^{-1}_{Pt} far superior to Pt/CNT (59.33 mA mg^{-1}_{Pt}) and CNT-free $Rh_5/Pt/SnO_2/CP$ (58.33 mA mg^{-1}_{Pt}). The electrooxidation of CO started at lower potentials on $Pt/SnO_2/CNT$ and $Rh_5/Pt/SnO_2/CP$. The

presence of two oxophilic materials SnO_2 and Rh, implies an earlier source of OH_{ads}-species, which aids the oxidation of adsorbed CO. The 3D porous structure, the binderless nature, the low amount of the noble catalyst, the excellent electroactivity and durability of the Rh_5/$PtSnO_2$/CNT/CP composite represent an important step forwarding in their use as anode electrocatalyst in commercial applications in DEFC.

Conflicts of interest

There are no conflicts to declare.

Acknowledgements

This work was supported by the Natural Sciences and Engineering Research Council of Canada (NSERC) and the Centre Québécois sur les Matériaux Fonctionnels (CQMF). H. Wang is grateful to China Scholarship Council for a PhD scholarship.

References

1 T. Ogawa, M. Takeuchi and Y. Kajikawa, *Sustainability*, 2018, **10**, 458–487.
2 E. Antolini, *J. Power Sources*, 2007, **170**, 1–12.
3 F. Vigier, C. Coutanceau, F. Hahn, E. Belgsir and C. Lamy, *J. Electroanal. Chem.*, 2004, **563**, 81–89.
4 J. Friedl and U. Stimming, *Electrochim. Acta*, 2013, **101**, 41–58.
5 Y. Wang, S. Zou and W.-B. Cai, *Catalysts*, 2015, **5**, 1507–1534.
6 L. Jiang, G. Sun, Z. Zhou, S. Sun, Q. Wang, S. Yan, H. Li, J. Tian, J. Guo and B. Zhou, *J. Phys. Chem. B*, 2005, **109**, 8774–8778.
7 L. Jiang, L. Colmenares, Z. Jusys, G. Sun and R. Behm, *Electrochim. Acta*, 2007, **53**, 377–389.
8 J. Silva, R. De Souza, L. Parreira, E. T. Neto, M. Calegaro and M. Santos, *Appl. Catal., B*, 2010, **99**, 265–271.
9 H. Zhang, C. Hu, X. He, L. Hong, G. Du and Y. Zhang, *J. Power Sources*, 2011, **196**, 4499–4505.
10 E. Higuchi, K. Miyata, T. Takase and H. Inoue, *J. Power Sources*, 2011, **196**, 1730–1737.
11 P. A. Russo, M. Ahn, Y.-E. Sung and N. Pinna, *RSC Adv.*, 2013, **3**, 7001–7008.
12 G. R. Salazar-Banda, H. B. Suffredini, L. A. Avaca and S. A. Machado, *Mater. Chem. Phys.*, 2009, **117**, 434–442.
13 V. Del Colle, J. Souza-Garcia, G. Tremiliosi-Filho, E. Herrero and J. M. Feliu, *Phys. Chem. Chem. Phys.*, 2011, **13**, 12163–12172.
14 E. P. Leão, M. J. Giz, G. A. Camara and G. Maia, *Electrochim. Acta*, 2011, **56**, 1337–1343.
15 M. Ahn, I. Y. Cha, J. K. Lee, S. J. Yoo and Y.-E. Sung, *J. Mater. Chem. A*, 2015, **3**, 17130–17134.
16 H.-B. Pan and C. M. Wai, *New J. Chem.*, 2011, **35**, 1649–1660.
17 T. F. M. Moreira, S. A. Neto, C. Lemoine, K. B. Kokoh, C. Morais, T. W. Napporn and P. Olivi, *RSC Adv.*, 2020, **10**, 35310–35317.
18 J. De Souza, S. Queiroz, K. Bergamaski, E. Gonzalez and F. Nart, *J. Phys. Chem. B*, 2002, **106**, 9825–9830.
19 F. Zhang, D. Zhou, Z. Zhang, M. Zhou and Q. Wang, *RSC Adv.*, 2015, **5**, 91829–91835.
20 Y. Shen, M. Z. Zhang, K. Xiao and J. Xi, *ChemCatChem*, 2014, **6**, 3254–3261.
21 L. Rao, Y.-X. Jiang, B.-W. Zhang, Y.-R. Cai and S.-G. Sun, *Phys. Chem. Chem. Phys.*, 2014, **16**, 13662–13671.
22 M. Li, A. Kowal, K. Sasaki, N. Marinkovic, D. Su, E. Korach, P. Liu and R. Adzic, *Electrochim. Acta*, 2010, **55**, 4331–4338.
23 M. Li, W.-P. Zhou, N. Marinkovic, K. Sasaki and R. Adzic, *Electrochim. Acta*, 2013, **104**, 454–461.
24 M. Li, D. A. Cullen, K. Sasaki, N. S. Marinkovic, K. More and R. R. Adzic, *J. Am. Chem. Soc.*, 2013, **135**, 132–141.
25 Z. Ramli and S. Kamarudin, *Nanoscale Res. Lett.*, 2018, **13**, 410–435.
26 S. Shahgaldi and J. Hamelin, *Carbon*, 2015, **94**, 705–728.
27 T. W. Odom, J.-L. Huang, P. Kim and C. M. Lieber, *J. Phys. Chem. B*, 2000, **104**, 2794–2809.
28 J.-P. Salvetat-Delmotte and A. Rubio, *Carbon*, 2002, **40**, 1729–1734.
29 L. Roen, C. Paik and T. Jarvi, *ECS Solid State Lett.*, 2003, **7**, A19–A22.
30 N. Macauley, D. D. Papadias, J. Fairweather, D. Spernjak, D. Langlois, R. Ahluwalia, K. L. More, R. Mukundan and R. L. Borup, *J. Electrochem. Soc.*, 2018, **165**, F3148–F3160.
31 L. Castanheira, W. O. Silva, F. H. Lima, A. Crisci, L. Dubau and F. d. r. Maillard, *ACS Catal.*, 2015, **5**, 2184–2194.
32 A. Tabet-Aoul and M. Mohamedi, *J. Mater. Chem.*, 2012, **22**, 2491–2497.
33 D. Geohegan, D. Chrisey and G. Hubler, in *Pulsed laser deposition of thin films*, ed. D. Chrisey and G. K. Hubler, Wiely, New York, 1994, pp. 59–69.
34 H. Wang, S. Sun and M. Mohamedi, *SN Appl. Sci.*, 2020, **2**, 1–9.
35 Y. Zhang, M. Janyasupab, C. W. Liu, X. Li, J. Xu and C. C. Liu, *Adv. Funct. Mater.*, 2012, **22**, 3570–3575.
36 M. L. Anderson, R. M. Stroud and D. R. Rolison, *Nano Lett.*, 2002, **2**, 235–240.
37 Y. Geng, M. Y. Liu, J. Li, X. M. Shi and J. K. Kim, *Composites, Part A*, 2008, **39**, 1876–1883.
38 J. Cui, Z.-L. Xu, S. Yao, J. Huang, J.-Q. Huang, S. Abouali, M. A. Garakani, X. Ning and J.-K. Kim, *J. Mater. Chem. A*, 2016, **4**, 10964–10973.
39 L. Zajíčková, Z. Kučerová, V. Buršíková, M. Eliáš, J. Houdková, P. Synek, H. Maršíková and O. Jašek, *Plasma Processes Polym.*, 2009, **6**, S864–S869.
40 J. Rojas, M. Toro-Gonzalez, M. Molina-Higgins and C. Castano, *Mater. Sci. Eng., C*, 2016, **205**, 28–35.
41 R. Tian, Y. Zhang, Z. Chen, H. Duan, B. Xu, Y. Guo, H. Kang, H. Li and H. Liu, *Sci. Rep.*, 2016, **6**, 19195–19203.
42 W. Wan, Y. Li, X. Ren, Y. Zhao, F. Gao and H. Zhao, *Nanomaterials*, 2018, **8**, 112–131.
43 S. Hussain, N. Kongi, H. Erikson, M. Rähn, M. Merisalu, L. Matisen, P. Paiste, J. Aruväli, V. Sammelselg and L. A. Estudillo-Wong, *Electrochim. Acta*, 2019, **316**, 162–172.
44 I. Jiménez-Morales, S. Cavaliere, D. Jones and J. Rozière, *Phys. Chem. Chem. Phys.*, 2018, **20**, 8765–8772.

45 M. Dou, M. Hou, D. Liang, W. Lu, Z. Shao and B. Yi, *Electrochim. Acta*, 2013, **92**, 468–473.
46 S. Meenakshi, P. Sridhar and S. Pitchumani, *RSC Adv.*, 2014, **4**, 44386–44393.
47 K. Ke and K. Waki, *J. Electrochem. Soc.*, 2007, **154**, A207–A212.
48 A. Ruban, B. Hammer, P. Stoltze, H. L. Skriver and J. K. Nørskov, *J. Mol. Catal. A: Chem.*, 1997, **115**, 421–429.
49 E. Christoffersen, P. Liu, A. Ruban, H. L. Skriver and J. K. Nørskov, *J. Catal.*, 2001, **199**, 123–131.
50 H. Wang, Z. Jusys and R. Behm, *J. Power Sources*, 2006, **154**, 351–359.
51 K. Kinoshita, D. Ferrier and P. Stonehart, *Electrochim. Acta*, 1978, **23**, 45–54.
52 T. Schmidt, H. Gasteiger, G. Stäb, P. Urban, D. Kolb and R. Behm, *J. Electrochem. Soc.*, 1998, **145**, 2354–2358.
53 A. B. Delpeuch, M. Chatenet, M. S. Rau and C. Cremers, *Phys. Chem. Chem. Phys.*, 2015, **17**, 10881–10893.
54 A. Pozio, M. De Francesco, A. Cemmi, F. Cardellini and L. Giorgi, *J. Power Sources*, 2002, **105**, 13–19.
55 X. Zhang, H. Zhu, Z. Guo, Y. Wei and F. Wang, *Int. J. Hydrogen Energy*, 2010, **35**, 8841–8847.
56 J. F. Gomes, B. Busson, A. Tadjeddine and G. Tremiliosi-Filho, *Electrochim. Acta*, 2008, **53**, 6899–6905.
57 Y. Wang, A. Tabet-Aoul, M. Gougis and M. Mohamedi, *J. Power Sources*, 2015, **273**, 904–913.
58 Y. E. Sung, S. Thomas and A. Wieckowski, *J. Phys. Chem.*, 1995, **99**, 13513–13521.
59 F. Maillard, F. Gloaguen, F. Hahn and J. M. Léger, *Fuel Cells*, 2002, **2**, 143–152.
60 H. Yuan, D. Guo, X. Li, L. Yuan, W. Zhu, L. Chen and X. Qiu, *Fuel Cells*, 2009, **9**, 121–127.
61 M. S. Saha, R. Li and X. Sun, *Electrochem. Commun.*, 2007, **9**, 2229–2234.
62 J. Jiang and A. Kucernak, *J. Electroanal. Chem.*, 2003, **543**, 187–199.

